

^7Li and ^6Li Solid-State NMR Studies of Structure and Dynamics in $\text{LiNbO}_3\text{--}\text{WO}_3$ Solid Solutions

Yin Xia,[§] Nobuya Machida,^{†,‡} Xuehua Wu,[#] Charles Lakeman,^{#,||} Leo van Wüllen,^{§,†} Fred Lange,[#] Carlos Levi,[#] and Hellmut Eckert^{§,†,*}

Departments of Materials and Chemistry, University of California, Santa Barbara, California 93106

Stanley Anderson

Westmont College, Santa Barbara, California 93108

Received: May 30, 1997; In Final Form: September 4, 1997[®]

The spatial distribution and atomic mobility of Li ions in the solid solution system $\text{Li}_{1-x}\text{Nb}_{1-x}\text{W}_x\text{O}_3$ ($0 \leq x \leq 0.5$) have been studied using solid-state NMR techniques. To maintain charge balance, for each tungsten atom substituting on a niobium site, a lithium vacancy is produced in the lithium sublattice. ^6Li magic angle spinning experiments reveal multiple lithium sites, attributed to distributions of niobium and tungsten neighbors. Dipolar ^7Li second moments measured at low temperature ($-100\text{ }^\circ\text{C}$) depend linearly on lithium content, consistent with a random distribution of vacancies. Variable temperature (-20 to $550\text{ }^\circ\text{C}$) ^7Li NMR studies as a function of composition give evidence for two distinct motional processes: at low temperatures (near $0\text{ }^\circ\text{C}$) a local hopping process involving only a minority of the lithium ions present is activated. At high temperatures ($300\text{ }^\circ\text{C}$ and above, depending on substitution levels) long-range diffusion involving all the lithium atoms is evident on the NMR time scale. As the substitution level x is increased, the long-range mobility of lithium increases. In contrast, the number of lithium atoms participating in the low-temperature process and their respective mobilities reach a maximum near $x = 0.25$. This result is explained on the basis of detailed simulations, considering favorable cation transport mechanisms through intrinsic vacancies of the LiNbO_3 lattice. Both the ^6Li line shape and the ^7Li dynamics simulations are consistent with a statistical distribution of Nb and W atoms and formation of W-vacancy pairs along the c -axis.

Introduction

Lithium niobate, LiNbO_3 , has attracted tremendous scientific and industrial interest because of its excellent electrooptical properties. Interesting potential applications include acoustic wave transducers, optical amplitude modulators, frequency doublers, waveguides, and holographic data processing devices.^{1–4} In particular, for second-harmonic generation, LiNbO_3 serves as a widely accepted standard against which new materials are being tested. Recently Wiegel and Blasse have found that this nonlinear response can be enhanced dramatically by substituting tungsten into the crystal structure of lithium niobate.⁵ They explain this effect by the higher polarizability of W–O bonds as compared to Nb–O bonds. The $(\text{LiNbO}_3)_{1-x}(\text{WO}_3)_x$ phase field is characterized by the existence of a stoichiometric compound $\alpha\text{-LiNbWO}_6$ ($x = 0.5$), possessing a new ordered trirutile structure and a wide solid solution range $0 \leq x \leq 0.5$ with the LiNbO_3 structure.^{5–7} Interestingly, substitution of Nb by W within this solid solution range only changes the c lattice parameter, leaving the a parameter unaltered. For this reason, epitaxial film growth of these solid solutions on undoped LiNbO_3 substrates is possible, opening up a variety of new optical waveguide applications. Accordingly, Lakeman et al. have recently reported a solution precursor method for the

growth of epitaxial $\text{Li}_{1-x}\text{Nb}_{1-x}\text{W}_x\text{O}_3$ thin films on basal plane single-crystal lithium niobate substrates.⁸

The tremendous interest of these new optical materials calls for a more detailed understanding of their structural organization and their dynamic properties. For example the spatial distribution of Nb and W atoms throughout the lattice has not been explored at this time, and therefore a structural explanation of the unidimensional change in the unit lattice constants is still outstanding. Furthermore, charge balance demands that each of the W atoms substituting on a Nb site also creates a vacancy in the lithium sublattice, resulting in a material that might be ionically conductive. Therefore, two central goals of this study are to elucidate the lithium/vacancy distributions and to confirm and characterize the expected ionic mobility in these solid solutions by suitable experimental probes.

Nuclear magnetic resonance (NMR) spectroscopy has proven to be a very powerful tool for the structural elucidation of disordered materials.⁹ Since NMR is element-selective, inherently quantitative, and focused on the effects of immediate nearest and next nearest neighbor environments, it can provide important information on the short-range order not available from X-ray powder diffraction experiments. Furthermore, since the local interactions affecting the NMR line shapes are modulated by atomic motion on the kHz time scale, NMR is a premier technique for characterizing slow atomic transport and molecular reorientations in the solid state.¹⁰ Past NMR studies of lithium niobate and tantalate have focused on a detailed characterization of the nuclear electric quadrupolar interaction of ^7Li and ^{93}Nb , with the primary goal of developing a structural description of nonstoichiometry in lithium niobate.^{11–15} Preliminary data concerning site distribution and atomic mobility of lithium have also been published for congruent and nonsto-

[§] Department of Chemistry.

[†] Present address: Institut für Physikalische Chemie, Westfälische Wilhelms-Universität, Münster, D48149 Münster, Germany.

[‡] Permanent address: Department of Chemistry, Konan University, Kobe 658, Japan.

[#] Department of Materials.

^{||} Present address: Advanced Materials Laboratory, 1001 University Blvd., SE, Albuquerque, NM 87105.

* Corresponding author.

[®] Abstract published in *Advance ACS Abstracts*, October 15, 1997.

TABLE 1: Elemental Compositions (Theoretical Values in Parentheses) and Crystallographic Lattice Parameters of Li_{1-x}Nb_{1-x}W_xO₃ Solid Solutions

<i>x</i>	weight %			<i>a</i> (Å)	<i>c</i> (Å)	cell vol. (Å ³)
	Li	Nb	W			
0.00				5.1519 ± 0.0015	13.8684 ± 0.0087	318.78 ± 0.18
0.10	3.78 (3.99)	52.93 (53.51)	11.88 (11.77)	5.1516 ± 0.0016	13.8481 ± 0.0093	318.28 ± 0.19
0.15	3.71 (3.68)	50.69 (49.21)	18.20 (17.19)	5.1530 ± 0.0022	13.8333 ± 0.0086	317.11 ± 0.20
0.20	3.26 (3.37)	44.67 (45.14)	21.26 (22.33)	5.1529 ± 0.0015	13.8123 ± 0.0091	317.62 ± 0.19
0.25	3.30 (3.08)	42.70 (41.26)	28.50 (27.22)	5.1529 ± 0.0012	13.7857 ± 0.0069	317.00 ± 0.14
0.30	2.76 (2.81)	37.21 (37.58)	30.94 (31.88)	5.1507 ± 0.0015	13.7677 ± 0.0113	316.33 ± 0.22
0.40	2.17 (2.29)	30.54 (30.72)	40.07 (40.53)	5.1539 ± 0.0015	13.7273 ± 0.0090	315.79 ± 0.19
0.50	1.90 (1.82)	24.26 (24.47)	48.58 (48.43)	5.1555 ± 0.0020	13.6771 ± 0.0098	314.83 ± 0.25

ichiometric lithium niobate^{15,16} and tantalate.¹⁷ In addition, the atomic distribution of various ternary solid solution systems has been examined on the basis of ⁷Li line shape analysis;¹⁸ however to the best of our knowledge, no solid-state NMR studies of lithium niobate–tungsten oxide solid solutions have appeared in the literature. The present paper presents a host of complementary experiments carried out on Li_{1-x}Nb_{1-x}W_xO₃ samples with variable substitution level *x*, resulting in a more detailed understanding of structure and ionic motion in these materials.

Experimental Section

Sample Preparation and Characterization. Samples with compositions Li_{1-x}Nb_{1-x}W_xO₃ (0 ≤ *x* ≤ 0.5) were prepared from Li₂CO₃ powder, 99.997%, Nb₂O₅ powder, 99.99%, and WO₃ powder, 99.995% (Aldrich). For compositions 0 ≤ *x* ≤ 0.15, the starting materials were heated in stoichiometric ratios at 800 °C for 12 h in air. At compositions 0.2 ≤ *x* ≤ 0.5 the preparation of single-phase materials required the use of 10% molar excess lithium carbonate. These samples were prepared in a two-step process: heating at 750 °C, 8 h, followed by milling, and reheating at 800 °C, 8 h in air. Preparation of isotopically enriched ⁶Li-containing samples followed the same procedure, except that ⁶Li-enriched Li₂CO₃ powder, 95 at. % ⁶Li (IsoTec), was used as a starting material. All the sample compositions were verified by chemical analysis for Li and Nb (Galbraith Laboratories, Inc., Knoxville, TN) and found to be very close to the batched compositions (see Table 1). Phase analysis was performed by high-resolution powder X-ray diffraction on a Scintag PAD-X instrument. Lattice parameters were determined by least-squares fit using silicon as an internal standard. As Table 1 reveals, the *a* parameter remains unaltered within experimental error, while the *c* parameter decreases with increasing *x*. This result agrees very well with the literature data.⁵ Small amounts (estimated to be less than 2%) of LiNb₃O₈ impurities were found at *x* = 0.1, 0.15, and 0.5; the latter material also contains a small amount (less than 2%) of Nb₂WO₈. Second harmonic generation measurements confirmed the linear increase of the corresponding coefficient with increasing *x*, as previously found.⁵

Nuclear Magnetic Resonance Measurements. Variable-temperature ⁷Li solid-state NMR experiments (−20 °C ≤ *T* ≤ 550 °C) were carried out at 116.793 MHz on static samples using a General Electric GN-300 spectrometer, equipped with a high-temperature NMR probe from Doty Scientific. Typical conditions were as follows: 90° pulses of 11–13 μs length and 5–20 s relaxation delays. In addition, low-temperature (−100 °C) NMR spin–echo experiments were conducted at 31.090 MHz, on a Bruker/IBM NR80 spectrometer, using a 90°–*t*₁–180°–*t*₁ pulse sequence. The 90° pulse lengths ranged from 9.3 to 9.5 μs on this spectrometer. The samples were allowed to equilibrate at a given temperature for 15–30 min. No appreciable temperature hysteresis effects were noticed under such conditions. ⁶Li MAS NMR spectra were obtained at 44.17 MHz, using a Bruker CXP-300 NMR spectrometer equipped

with a TECMAG pulse programmer and acquisition system and a 4 mm high-speed MAS probe. Typically 16 scans were acquired with 90° pulses of 5 μs length, relaxation delays of 200 s, and 10 kHz spinning speed. In addition, ¹⁸³W NMR experiments were attempted on a Bruker DSX 500 spectrometer at 20.837 MHz, using 7 mm spinners at 5–6 kHz spinning speed. Using 40° pulses of 6 μs length and relaxation delays of 30–100 s, it was possible to obtain ¹⁸³W NMR signals of the standard compounds WO₃ and Li₂WO₄ with 400 scans at signal-to-noise ratios comparable to those reported in the literature,¹⁹ while no signal at all was detectable for Li_{0.5}Nb_{0.5}W_{0.5}O₃ solid solution with 1520 scans using similar conditions.

Results, Data Analysis, and Interpretation

⁷Li Spin–Echo NMR. One question of interest in the context of the present study concerns the spatial distribution of Li, vacancies, Nb, and W species in the solid solution system. Due to their rigorous dependence on interatomic distances ⁷Li–⁷Li dipole–dipole coupling strengths can give important information on this issue. For example, a statistical lithium distribution gives a weaker average dipole–dipole coupling than a distribution into LiNbO₃ and WO₃ cluster domains. While the ⁷Li spin Hamiltonian contains many different contributions, including homo- and heterodipolar interactions, chemical shielding, and nuclear electric quadrupolar coupling, a selective NMR measurement of the ⁷Li–⁷Li dipole–dipole couplings can be accomplished by the Hahn spin–echo decay technique, as previously discussed.²⁰ For a crystalline compound with multiple spin interactions, a Gaussian decay of the normalized spin–echo intensity is expected as a function of evolution time,

$$I/I_0 = \exp[-((2t_1)^2 M_2(^7\text{Li}-^7\text{Li})/2)]$$

where *M*₂(⁷Li–⁷Li) is the second moment characterizing the strength of the internuclear homodipolar coupling. The experimental data can be compared with calculated values expected from various atomic distribution models using van Vleck theory.²¹

$$M_2 = (4/15)(\mu_0/4\pi)^2 \gamma^4 \hbar^2 I(I+1) \sum_{i \neq j} r_{ij}^{-6}$$

In this expression, the lattice sum over the inverse sixth power of the internuclear distances *r*_{*ij*} is the decisive structural parameter. All the other terms, including *γ* and *I*, the gyromagnetic ratio and the spin quantum number of the ⁷Li isotope, are physical constants. To ensure that the spin–echoes are not affected by atomic motion occurring on the time scale of the experiments, these studies have to be conducted in the rigid lattice limit, which in our materials is attained at temperatures near −100 °C. This approach is rigorously applicable only if the differences between the resonance frequencies of neighboring spins are larger than the frequency characterizing the strength of their dipole–dipole coupling, thus eliminating the contribution of flip-flop transitions (*B* term of the dipolar Hamiltonian)

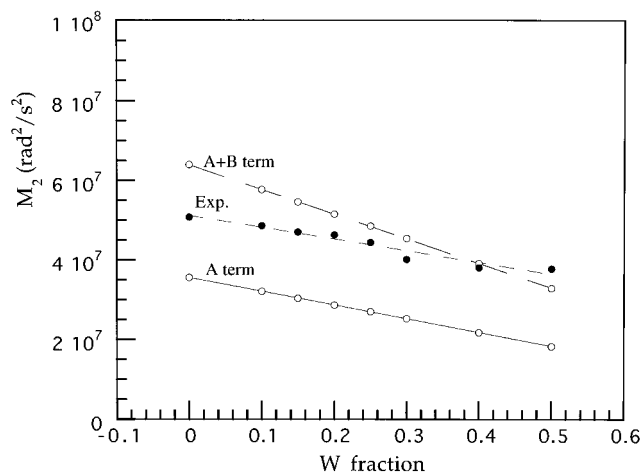


Figure 1. Second moments $M_2(^7\text{Li}-^7\text{Li})$ of $\text{Li}_{1-x}\text{Nb}_{1-x}\text{W}_x\text{O}_3$ solid solutions. Experimental data (full circles) are contrasted with van Vleck calculations in the limit of spin exchange totally suppressed (A term of the dipolar Hamiltonian) and fully active (A + B term of the dipolar Hamiltonian).

to the second moment. If the latter condition is not fulfilled, apparently higher experimental M_2 values are measured; however, the theory is only approximately applicable under these conditions.²² Figure 1 contrasts experimental data to predicted M_2 values for completely suppressed flip-flop transitions (lower line) and fully activated flip-flop transitions (upper line). (For the latter case, it is not clear, however, how well the predictions can be realized by the spin-echo decay experiments; see discussion above). Already in pure LiNbO_3 , the experimental M_2 value lies between those calculated for the two extreme cases, suggesting that an intermediate situation holds, in which flip-flop transitions contribute at least partially. Figure 1 shows this to be the case within the entire solid solution range. Despite this difficulty, the experimentally observed trend in the data is instructive: the $M_2(^7\text{Li}-^7\text{Li})$ values measured by the spin-echo technique appear to depend linearly on x . This monotonic behavior is qualitatively consistent with a statistical distribution of lithium atoms and argues against strong clustering of LiNbO_3 and WO_3 domains.

^6Li MAS NMR. Substitution of W on the Nb sites creates multiple lithium next-nearest neighbor environments which should, in principle, be characterized by different chemical shift values. To resolve the latter, high-resolution solid-state NMR methods, notably magic angle spinning (MAS) is necessary. Previous work has shown that the fairly strong homonuclear $^7\text{Li}-^7\text{Li}$ dipole-dipole couplings are not completely averaged out at typical MAS spinning speeds, thereby limiting the resolution attainable. In contrast, the other isotope, ^6Li , offers substantially improved resolution due to its smaller magnetic dipole moment and its smaller nuclear electric quadrupolar coupling constant.^{23,24} Figure 2 shows the ^6Li MAS NMR spectra as a function of composition. Spectral deconvolution reveals the presence of at least three components with fairly consistent line shape parameters (Figure 3). The respective peak positions, widths, and area fractions are summarized in Table 2.

^7Li Variable-Temperature NMR. Charge balance dictates that in $\text{Li}_{1-x}\text{Nb}_{1-x}\text{W}_x\text{O}_3$ the concentrations of W and induced vacancies are equal. Since these vacancies facilitate the movement of lithium ions, one would expect an increase in the lithium mobility with increasing tungsten content. This effect can be probed by variable-temperature ^7Li NMR, because the $^7\text{Li}-^7\text{Li}$ and $^7\text{Li}-^{93}\text{Nb}$ dipole-dipole interactions, as well as nuclear electric quadrupolar couplings, are modulated by atomic motion at frequencies comparable to the static line width

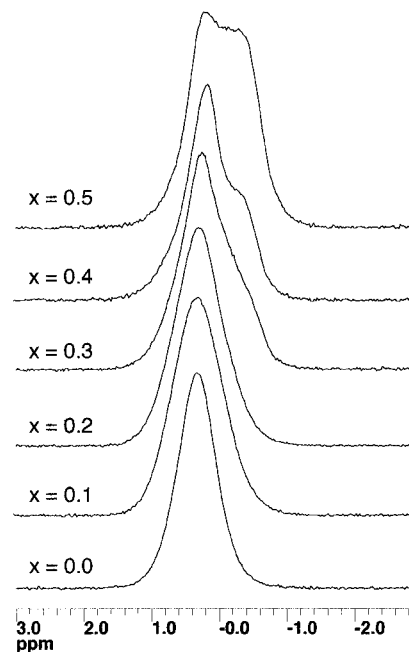


Figure 2. Compositional evolution of the ^6Li MAS NMR spectra of $\text{Li}_{1-x}\text{Nb}_{1-x}\text{W}_x\text{O}_3$ solid solutions.

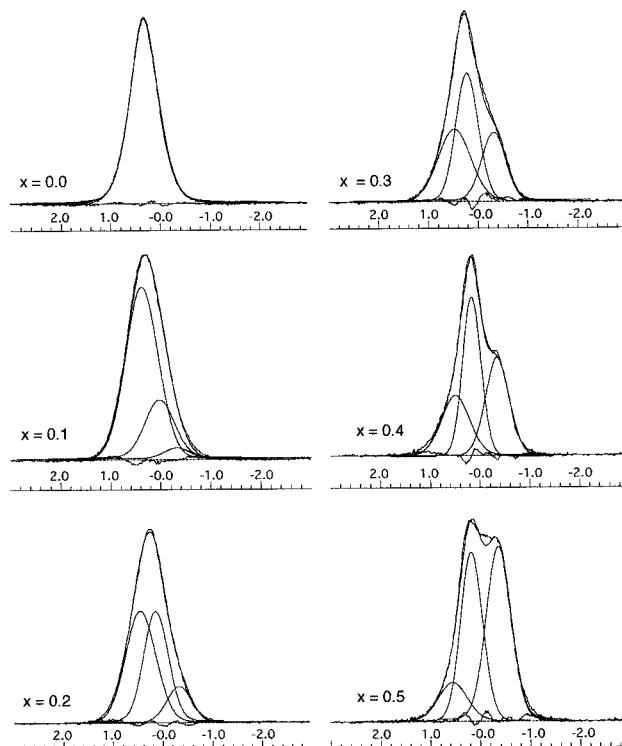


Figure 3. Deconvolution of the ^6Li MAS NMR spectra of $\text{Li}_{1-x}\text{Nb}_{1-x}\text{W}_x\text{O}_3$ solid solutions into Gaussian components. Differences between experimental and simulated spectra are indicated.

(typically several kHz), resulting in *motional narrowing* of the spectral lines with increasing temperature. Figure 4 summarizes representative data from variable-temperature ^7Li NMR. Shown is only the dominant central peak, corresponding to the $m = 1/2 \leftrightarrow -1/2$ transition, whereas the $m = 3/2 \leftrightarrow 1/2$ and the $m = -1/2 \leftrightarrow -3/2$ satellite transitions are shifted and broadened due to the anisotropy of the quadrupolar interactions and are thus not observed under these conditions.

Figure 4 illustrates that at temperatures below 400 °C the spectra are generally comprised of a broad component, attributable to immobile lithium, and a narrow component reflecting lithium species that are highly mobile. Inversion recovery experiments indicate that both types of lithium have distinct

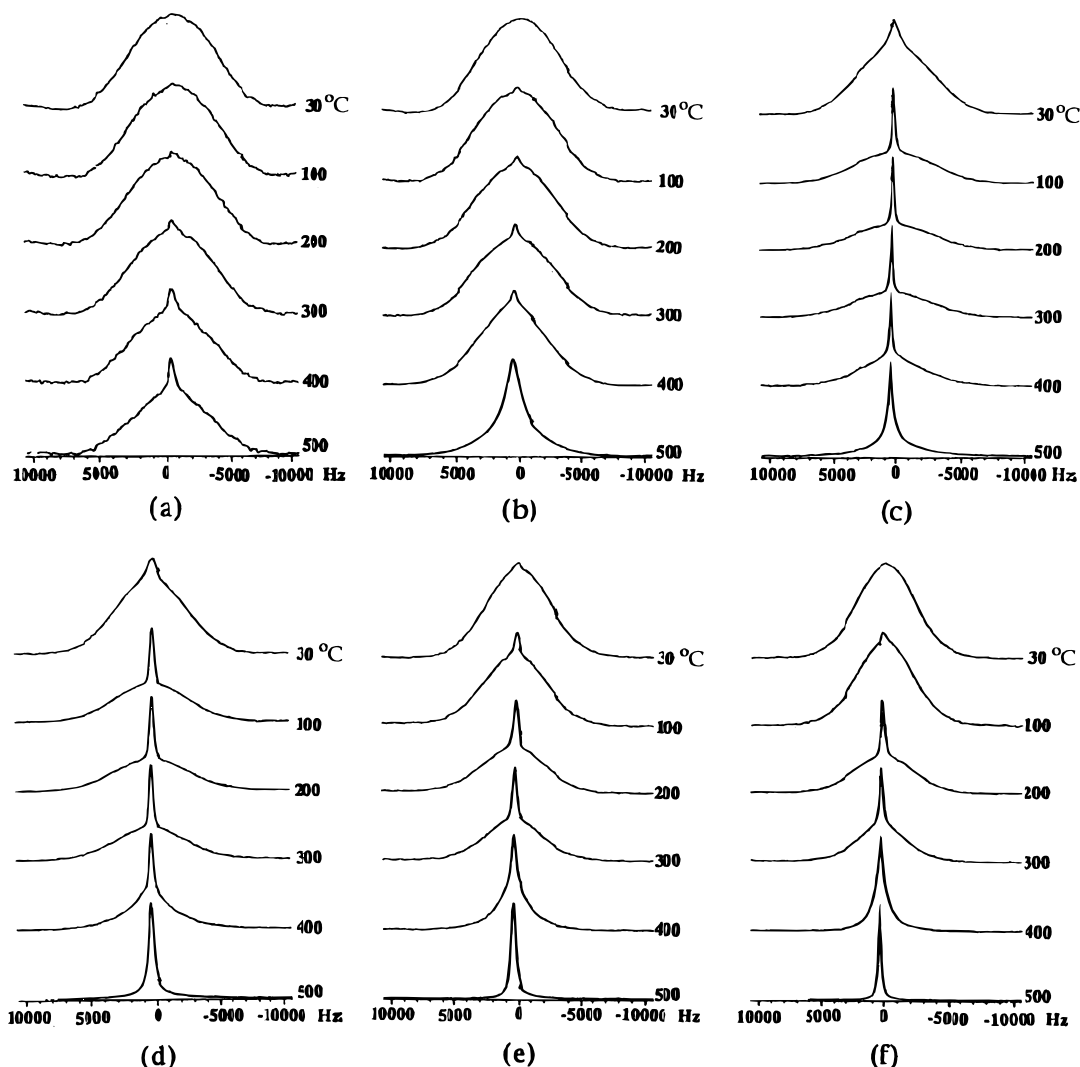


Figure 4. Variable-temperature ^7Li NMR spectra of $\text{Li}_{1-x}\text{Nb}_{1-x}\text{W}_x\text{O}_3$ solid solutions: (a) $x = 0$, (b) $x = 0.1$, (c) $x = 0.2$, (d) $x = 0.3$, (e) $x = 0.4$, (f) $x = 0.5$.

TABLE 2: Peak Positions, Relative Intensities, and Full Width at Half-Maximum (fwhm) of the ^6Li MAS NMR Spectra of $\text{Li}_{(1-x)}\text{Nb}_{(1-x)}\text{W}_x\text{O}_3$ Solid Solutions

sample x	peak position/ppm			relative intensity/%			fwhm/Hz		
	peak 1	peak 2	peak 3	peak 1	peak 2	peak 3	peak 1	peak 2	peak 3
0.0	0.33			100	0.0	0.0	37.9		
0.1	0.37	0.02	-0.32	73.6	22.6	4.0	39.8	33.4	29.1
0.2	0.46	0.15	-0.31	49.2	38.2	12.6	37.9	29.9	31.1
0.3	0.48	0.22	-0.31	34.2	42.1	23.7	39.8	28.2	30.3
0.4	0.49	0.16	-0.35	24.0	42.7	33.3	35.6	23.8	30.3
0.5	0.57	0.18	-0.36	12.3	39.8	47.8	35.7	27.3	30.8

spin–lattice relaxation times, differing by approximately 1 order of magnitude from each other over the entire temperature range investigated. These experiments reveal that the NMR line shapes arise from two separate lithium populations, which are not in spin-diffusion contact with each other. The spectra were deconvoluted into a broad Gaussian and a narrow Lorentzian contribution and the respective parameters optimized by a nonlinear least-squares analysis procedure using the Levenberg–Marquardt method. For all of the samples except $x = 0.5$, this decomposition is possible at temperatures below 300 °C, while at higher temperatures the distinction between broad and sharp lines is increasingly blurred, because the majority lithium sites are now also experiencing motional narrowing. Table 3 summarizes the results of this analysis. Figure 5 shows how the area fraction of the sharp line depends on the W substitution level and the temperature in the low-temperature region. At each composition the area fraction of the narrow peak initially

TABLE 3: Contribution of the Sharp Line to the Total Area (in Percent) of the ^7Li Solid-State NMR Spectra of $\text{Li}_{1-x}\text{Nb}_{1-x}\text{W}_x\text{O}_3$ Solid Solutions as a Function of x and Temperature

x	30 °C	50 °C	100 °C	150 °C	200 °C	250 °C	300 °C
0.00	0	0	0	0	0.1	0.3	0.6
0.10	0	0	0	0.3	0.6	0.7	0.9
0.15	0	0	0.7	1.0	2.0	2.3	4.0
0.20	3.7	5.8	10.1	10.8	13.0	13.6	13.6
0.25	6.0	8.0	11.8	15.9	17.1	17.1	16.7
0.30	2.8	5.1	8.2	9.2	9.5	10.2	10.9
0.40	0.7	1.2	2.3	4.0	6.5	7.7	8.5
0.50	0.2	0.2	1.1	<i>a</i>	<i>a</i>	<i>a</i>	<i>a</i>

^a Distinction between broad and sharp line not possible.

increases with increasing temperature and reaches a plateau value within the temperature range $200 \leq T \leq 300$ °C. Interestingly, the plateau value reveals a pronounced maximum

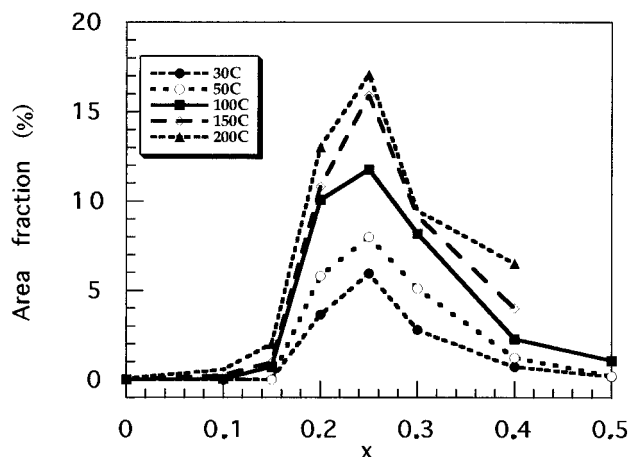


Figure 5. Area fraction of the sharp ${}^7\text{Li}$ NMR line shape component in the spectra of $\text{Li}_{1-x}\text{Nb}_{1-x}\text{W}_x\text{O}_3$ solid solutions as a function of x and temperature.

near the composition $x = 0.25$ (see Table 3 and Discussion below). We attribute the sharp line to a distinct population of highly mobile lithium species, involved in a low activation energy process. It should be noted that the fractions of these lithium species are probably lower than estimable from the area fractions given in Figure 5. If these lithium species are isotropically mobile, the nuclear electric quadrupolar splitting would be removed, and the sharp line then constitutes the sum of three degenerate $|\Delta m| = 1$ transitions. In contrast, the broad line represents only the central $m = 1/2 \leftrightarrow m = -1/2$ transition, which accounts for only 40% of the total lithium species of this type.

Finally, Figure 6 shows the temperature dependence of the width of the broad component constituting the majority of the lithium ions. While these species are rigid at room temperature in all of the samples studied, motional narrowing is observed at elevated temperatures, such that no distinction between sharp and broad line shape components is evident at temperatures of 400 °C and above. From the onset temperature of motional narrowing, T_c , we can estimate the activation energies for both the high- and low-temperature processes via the Waugh–Fedin expression:²⁵

$$E_a \text{ (kJ/mol)} = 0.156T_c \text{ (K)}$$

(In the case of the low-activation energy process the temperature at which the sharp line appears first is taken as T_c). Figure 7 illustrates that the activation energies of the high-temperature process decrease continuously with increasing substitution level x , making a sharp drop near $x = 0.50$. In contrast, the activation energy of the low-temperature process shows a local minimum near $x = 0.25$. At composition $x = 0.50$, no clear distinction is possible between both processes above 200 °C.

Discussion

Cation Distribution and Local Surroundings. The solid-state chemistry of lithium niobate and of the solid solutions derived from this material has been reviewed extensively. There is now a general consensus that nonstoichiometric solid solutions based on lithium niobate possess an intact oxygen framework, while charge neutrality is maintained exclusively by adjustment of occupancies of the cation sites.^{26,27} Therefore the structural discussion of the lithium niobate/tungsten oxide solid solution system will focus on the overall spatial distribution of the Li^+ , Nb^{5+} , and W^{6+} ions within the cation sublattice and the local surroundings of these ions by the cationic next nearest neighbors. The monotonic decrease of ${}^7\text{Li}$ low-temperature second-moment

data with increasing x confirms that, on the whole, the lithium ions are statistically distributed throughout the solid solution. Further information on the local surroundings (short-range order) of the lithium ions in the solid solution lattice can be obtained from the ${}^6\text{Li}$ MAS NMR data. In the LiNbO_3 structure, each lithium site is octahedrally coordinated by oxygen and possesses four Nb next nearest neighbors. Therefore, partial substitution by W can result in five distinct possible sites, corresponding to 4Nb, 3Nb and 1W, 2Nb and 2W, 1Nb and 3W, and 4W atoms in the second coordination shell. The quantitative populations of these environments depend on the structural organization of these solid solutions. If maximum entropy is the driving force, then these populations are simply governed by binomial statistics. On the other hand, if minimization of the local charge is the driving force, then one expects that the W and vacancy sites attract each other mutually, leading to a preferential surrounding of lithium by niobium atoms, up to the extreme situation that the number of W atoms in the next nearest neighbor environment of lithium is as small as possible. Figure 8 illustrates the quantitative predictions for three scenarios as detailed below.

Scenario I. A statistical distribution model was simulated as follows: a perfect crystal of LiNbO_3 was generated in the computer. This crystal consisted of $30 \times 30 \times 30$ Li–Nb–V arrays, thereby including 27 000 unit cells. Using a random number generator, Nb atoms were replaced by W atoms at random, according to the substitution level x considered. In a separate, independent step, the same number of Li sites were randomly replaced by vacancies. No preferential interactions between W atoms and vacancies were considered. Following this process, the populations of the five possible lithium environments were counted.

Scenario II. A model corresponding to maximized W \leftrightarrow vacancy interactions was generated with the assumption that the stability of the lithium next nearest neighbor environments follows the order $4\text{W}, 0\text{Nb} < 3\text{W}, 1\text{Nb} < 2\text{W}, 2\text{Nb} < 1\text{W}, 3\text{Nb} < 4\text{Nb}$. Following the random replacement of Nb sites by W sites (according to the x value chosen), the next nearest neighbor surroundings of the Li sites were examined. Lithium atoms in the less stable sites were then successively replaced by vacancies, following the order of stability given above, until the lattice possessed the same number of vacancies as W atoms.

Scenario III. In this scenario, termed “ c -axis model”, each of the randomly placed W sites is accompanied by a vacancy in the site directly above, along the c -axis. This model appears particularly plausible because of the strong effect of W substitution on the c lattice parameter and because the shortest interatomic Li–Nb distance is along the c -axis.

Figure 3 shows that satisfactory and consistent fits to the ${}^6\text{Li}$ MAS NMR spectra can be obtained assuming only three spectral components. This result argues against scenario I and in favor of preferred W \leftrightarrow vacancy interactions. The peak position near 0.45 ± 0.12 ppm can be assigned to lithium surrounded by 4Nb next nearest neighbors, the resonance near 0.12 ± 0.10 ppm to lithium in a 3Nb, 1W environment, and the resonance near -0.33 ± 0.03 ppm to the Li site in the 2Nb, 2W environment. Overall, the experimental Li fractions and their dependence on x show better quantitative agreement with scenario III than scenarios I and II. As shown in the bottom part of each figure, the agreement of the experimental data with the prediction from scenario III is particularly good if the assumption is made that the lowest frequency line in the experimental spectra actually comprises the three types of environments 2Nb, 2W; 1Nb, 3W; and 4W.

Finally, the results of Figure 8 clearly rule out a final possibility, namely that $\text{Li}_{0.5}\text{Nb}_{0.5}\text{W}_{0.5}\text{O}_3$ possesses a super-

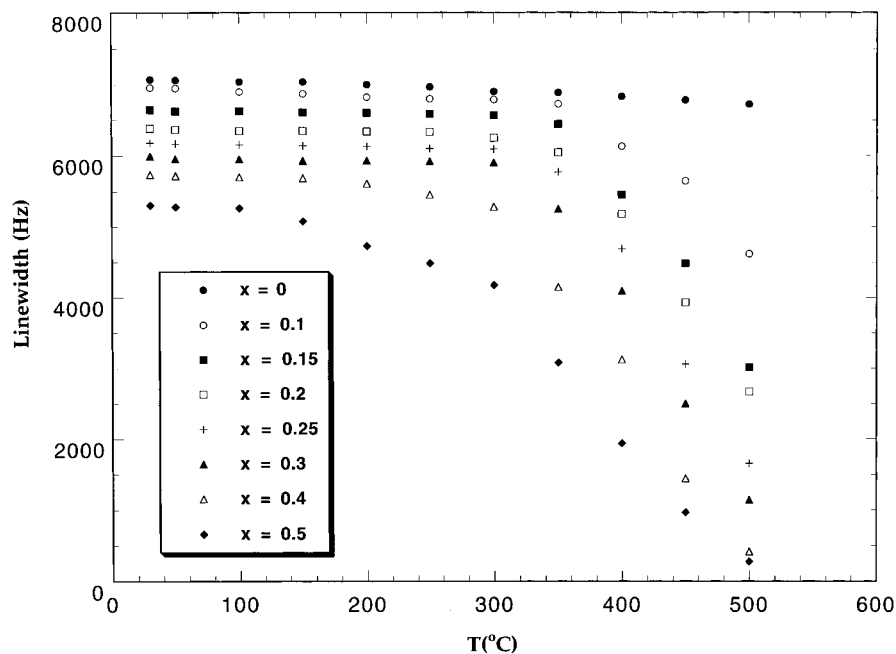


Figure 6. Full width at half-maximum of the broad ^7Li NMR line shape component in the spectra of $\text{Li}_{1-x}\text{Nb}_x\text{W}_x\text{O}_3$ solid solutions as a function of x and temperature.

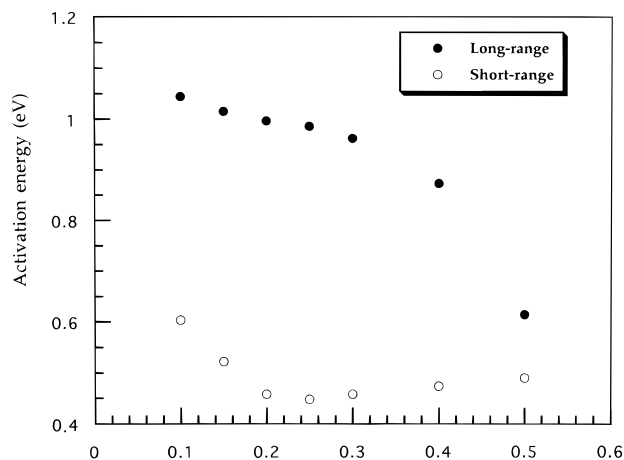


Figure 7. Activation energies associated with the high- and low-temperature processes in $\text{Li}_{1-x}\text{Nb}_x\text{W}_x\text{O}_3$ solid solutions.

structure. In the latter case, only a single lithium site would be expected, corresponding to a 2W,2Nb next nearest neighbor environment. In addition, both X-ray powder diffraction and transmission electron microscopy studies reveal no evidence whatsoever of structural ordering in these solid solutions.

In principle, it would be important to verify the above conclusions about the metal ion site distributions by complementary NMR studies of the nuclei ^{93}Nb and ^{183}W . Unfortunately, however, the ^{93}Nb NMR spectra of these samples are plagued by strong second-order quadrupolar broadening effects ($I = 9/2$), resulting in ill-defined spectra for the solid solutions with $x > 0.1$. Also, all our attempts at obtaining ^{183}W spectra, both by the Bloch decay method and by cross polarization from ^7Li , have been unsuccessful.

Lithium Ionic Motion. One of the interesting features of the present solid solution samples is the clear spectroscopic distinction between minority lithium species that appear to be highly mobile at low temperatures and the majority of the lithium atoms that become mobile on the NMR time scale only at elevated temperatures. The increase of the mobility of the majority lithium sites with increasing x can be easily understood in terms of the increased number of vacancies introduced by tungsten substitution. A similar effect has been observed by

electrical conductivity measurements in the solid solution system $\text{LiTaO}_3\text{--WO}_3$.²⁸

Perhaps surprising is the distinct maximum at $x = 0.25$ in the number of lithium species that contribute to the low-temperature, low activation energy process (Figure 5). To rationalize this phenomenon, a more detailed consideration of the mechanism of lithium migration in the lithium niobate lattice is necessary.²⁹ In this context it is important to consider the fact that, in addition to the occupied octahedral sites, the lithium niobate structure provides additional intrinsic octahedral vacancies as well as tetrahedral vacancies that are, in principle, available for the ionic transport in lithium niobate crystals. Figure 9 shows an example of the likely migration path for Li ions in the a,b basal plane of LiNbO_3 . Each arrow corresponds to a jump during which the lithium ion pushes through oxygen triangles when moving between octahedral and tetrahedral sites. All the migration paths in the basal plane must pass through similar oxygen constrictions, the intrinsic octahedral vacancy. In addition, direct jumps along the c -axis are possible.

In LiNbO_3 , the intrinsic octahedral vacancy is surrounded by a total of eight next nearest neighbor cations. Of these, three Nb and three Li reside in the a,b basal plane and one Li and Nb each are found along the c -axis. In the $\text{Li}_{1-x}\text{Nb}_{1-x}\text{W}_x\text{O}_3$ solid solutions a Nb could be replaced by a W atom (W_{Nb}) and the Li could be replaced by a vacancy (V_{Li}). Each W^{6+} on a Nb^{5+} site carries a net positive charge, and each vacancy on a Li^+ site carries a net negative charge. Thus, from the number of individual Nb_{Nb} , Li_{Li} , W_{Nb} , and V_{Li} sites in the next nearest neighbor environment one can attribute a local charge to this intrinsic site. We propose that this charge determines the likelihood with which this intrinsic vacancy will participate in Li^+ transport. Positive local charges will repel the lithium ions, while negative local charges will lead to trapping; both mechanisms will suppress lithium transport, at least at low temperatures. Thus, lithium motion will be supported only by intrinsic vacancies possessing zero local charge. The latter are found at the following next nearest neighbor cation configurations A through E (Figure 10), where A = 4Nb,4Li; B = 3Nb,1W,3Li,1V; C = 2Nb,2W,2Li,2V; D = 1Nb,3W,1Li,3V; and E = 4W,4V. Of these, the configuration A and E are dropped from consideration, because A provides no vacancy site for

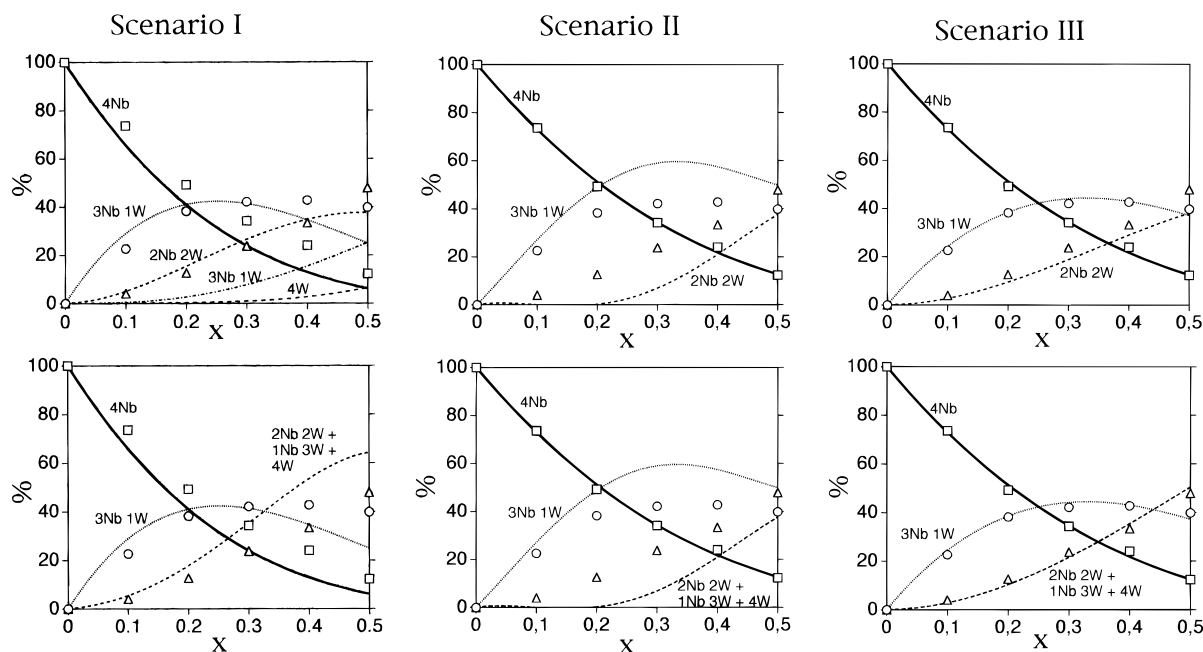


Figure 8. Comparison of experimental lithium site populations with those predicted from scenarios I–III (see text). Top: Only the three most favorable sites are considered: squares, 4Nb environments; circles, 3Nb,1W environments. Solid, dashed, and dotted curves denote predictions based on simulations. Bottom: All possible sites are considered, and for calculation of the simulated curves the assumption is made that the lowest frequency ^6Li NMR line near -0.33 ppm comprises the next nearest neighbor environments 2W,2Nb as well as 3W,1Nb.

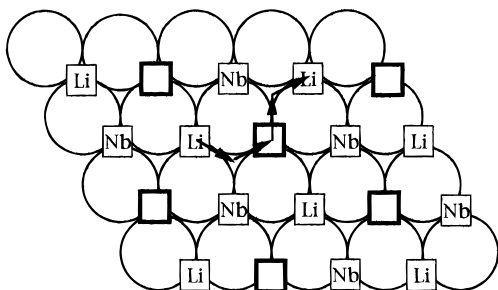


Figure 9. Likely migration path for Li in LiNbO_3 , illustrating the role of intrinsic vacancies.

lithium to jump into, while E contains no mobile lithium.

The relative concentrations of these different types of intrinsic vacancies were calculated for the three different scenarios I–III, and the results are summarized in Figure 11, top. With respect

to this question, simulations according to scenarios I and III produce identical results; note in particular the distinct maximum in the concentration of B sites for $x = 0.25$. In contrast, scenario II does not predict such a maximum.

With this information in hand, we can now estimate the fraction of mobile Li atoms pushing through the favorable intrinsic vacancy sites. This fraction is calculated according to

$$f(\text{mobile Li}) = (3f_B + 2f_C + f_D) \times 1/4$$

In this equation, the prefactors 1, 2, and 3 denote the number of Li atoms surrounding each site, while the factor 1/4 takes into account the fact that each Li atom is surrounded by four intrinsic vacancies. Figure 11, bottom, shows the composition dependence of the relative amounts of mobile Li ions calculated in this way for each scenario. Although the model cannot reproduce the fraction of mobile lithium ions quantitatively, the

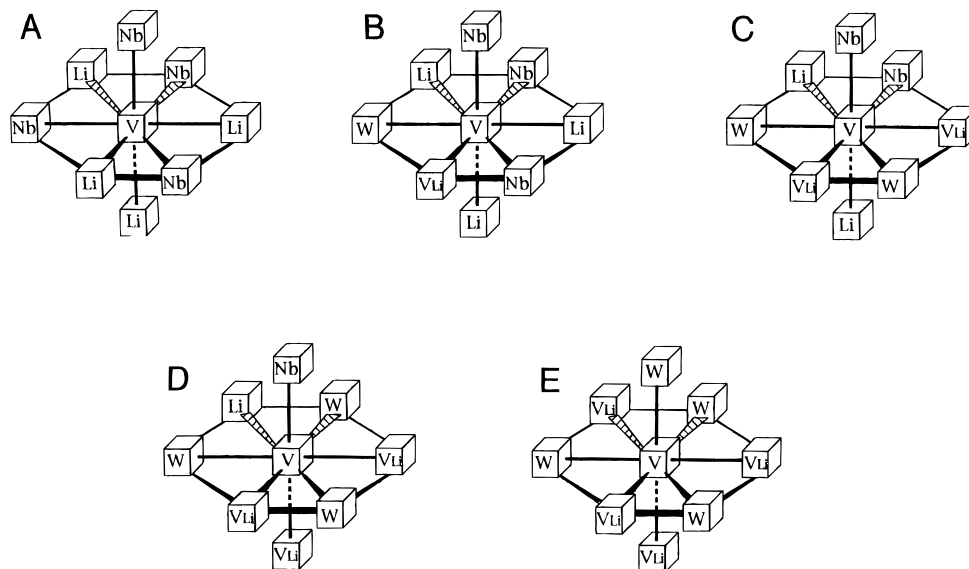


Figure 10. The five next nearest neighbor environments of intrinsic vacancies possessing zero local charge in $\text{Li}_{1-x}\text{Nb}_{1-x}\text{W}_x\text{O}_3$ solid solutions (sites A–E).

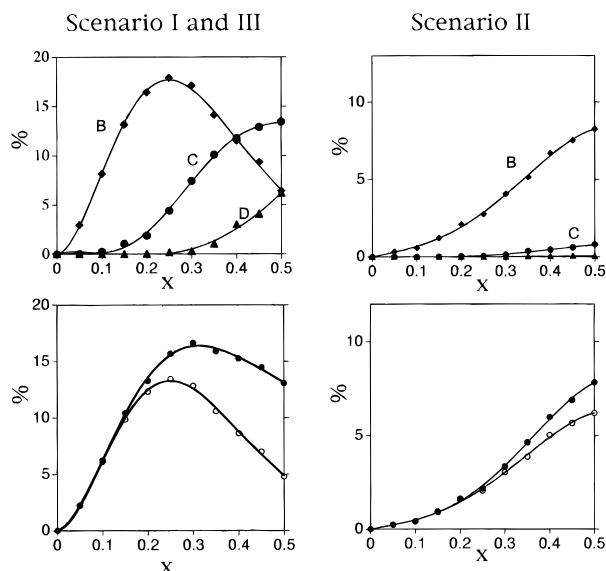


Figure 11. Top: Relative concentrations of sites B, C and D as calculated from scenarios I–III in $\text{Li}_{1-x}\text{Nb}_{1-x}\text{W}_x\text{O}_3$ solid solutions (see text for details). Bottom: Relative concentrations of Li⁺ ions accessible to a preferential migration path for the three cation ordering scenarios considered in this study (see text for details): closed circles, Li⁺ ions near B-type sites only; open circles, Li⁺ ions near sites of type B, C, and D.

figure nevertheless illustrates a relative maximum near the $x = 0.25$ composition for both scenarios I and III, in agreement with the trend evident in the experimental data. The agreement with the experimental data is even better if one assumes that cation mobility at low temperatures is preferentially maintained by vacancy sites of type B (open symbols in Figure 11). While all of the data clearly discriminate against scenario II, a distinction between scenarios I and III is not possible on the basis of the ⁷Li variable-temperature NMR data. Note, however, that the ⁶Li MAS NMR data are clearly supportive of the “c-axis” model (scenario III).

We note that the above considerations about lithium motion across particularly favorable intrinsic vacancy sites apply only at very low temperatures. Since, particularly at low substitution levels, these intrinsic vacancy sites are most probably isolated from each other, the motion must be considered as locally restricted rather than as contributing to cation transport. At higher temperatures, cation transport can proceed as less favorable vacancy sites become thermally accessible, and the distinction between the low activation energy process and the high activation energy process is gradually lost.

Conclusions

In summary, a cation distribution model for the solid solution system lithium niobate/tungsten trioxide, $\text{Li}_{1-x}\text{Nb}_{1-x}\text{W}_x\text{O}_3$, has been proposed on the basis of experimental evidence from X-ray powder diffraction and solid-state NMR spectroscopy. These NMR data differentiate between various alternative ordering models. In the model most consistent with ⁶Li high-resolution solid-state NMR data, the W atoms replace Nb sites at random and are associated with vacancies in the Li sublattice along the direction of the crystallographic *c*-axis. Static ⁷Li NMR spectra obtained as a function of temperature indicate that W substitution increases the cationic mobility of lithium. Two distinct motional

processes are evident in the data: a low-temperature, low activation energy process involving only a small fraction of lithium atoms and a high-activation energy process to which all of the lithium atoms contribute at high temperatures. The activation energy of the high-temperature process decreases with increasing substitution level x ; the increased lithium mobility presumably reflects the increase in the number of vacancies in the lithium sublattice. Concerning the low-temperature process, a relative maximum in the lithium mobility is observed at the composition $x = 0.25$. This, perhaps unexpected, observation can be explained by considering the likely migration path of the lithium ions, which includes the intrinsic octahedral vacancy sites in the LiNbO₃ lattice. As shown by detailed simulations, a random W placement with associated vacancies along the *c*-axis indeed generates a maximum of locally mobile lithium ions for $x = 0.25$, in agreement with the experimental result. Overall, the present study illustrates the power and potential of solid-state NMR methods to provide intricate information on the structure and dynamics of crystalline solid solution systems.

Acknowledgment. This project was sponsored by the Materials Research Laboratory at the University of California, Santa Barbara, under Grant No. DMR-9123048 from the National Science Foundation. The program manager is Dr. Lance Haworth.

References and Notes

- (1) Abouelleil, M.; Leonberger, F. *J. Am. Ceram. Soc.* **1989**, 72, 1322.
- (2) Sohler, W. *Thin Solid Films* **1989**, 175, 191.
- (3) Matthews, P.; Mickelson, A.; Novak, S. *J. Appl. Phys.* **1992**, 72, 2562.
- (4) Furukawa, Y.; Sato, M.; Minakata, M. *J. Appl. Phys.* **1992**, 72, 3250.
- (5) Weigel, M.; Emond, M. H. J.; DeBruin, T. H. M.; Blasse, G. *Chem. Mater.* **1994**, 6, 973.
- (6) Fourquet, J. L.; Le Bail, A.; Gillet, P. A. *Mater. Res. Bull.* **1988**, 23, 1163.
- (7) Blasse, G.; dePauw, A. D. M. *J. Inorg. Nucl. Chem.* **1970**, 32, 3960.
- (8) Lakeman, C. D. E.; Xia, Y.; Kim, J. H.; Wu, X.; Speck, J. S.; Eckert, H.; Lange, F. F. *J. Mater. Res.*, in press.
- (9) Eckert, H. *Prog. Nucl. Magn. Reson. Spectrosc.* **1992**, 24, 159.
- (10) Göbel, E.; Olyschläger, H.; Müller-Warmuth, W.; Dutz, H. *J. Magn. Reson.* **1979**, 36, 371.
- (11) Peterson, G. E.; Bridenbaugh, P. M. *J. Chem. Phys.* **1968**, 48, 3402.
- (12) Peterson, G. E.; Bridenbaugh, P. M.; Green, P. J. *J. Chem. Phys.* **1967**, 46, 4009.
- (13) Douglass, D. C.; Peterson, G. E.; McBrierty, V. J. *Phys. Rev. B* **1989**, 40, 10694.
- (14) Burns, G. *Phys. Rev.* **1962**, 127, 1193.
- (15) Halstead, T. K. *J. Chem. Phys.* **1970**, 53, 3427.
- (16) Blümel, J.; Born, E.; Metzger, T. *J. Phys. Chem. Solids* **1994**, 55, 589.
- (17) Allemann, J. A.; Xia, Y.; Morriss, R. E.; Wilkinson, A. P.; Eckert, H.; Speck, J. S.; Levi, C. G.; Lange, F. F. *J. Mater. Res.* **1996**, 11, 2376.
- (18) Ravez, J.; Joo, G. T.; Senegas, J.; Hagenmuller, P. *Jpn. J. Appl. Phys.* **1985**, 24, 1000.
- (19) Knight, C. T. G.; Turner, G.; Kirkpatrick, R. J.; Oldfield, E. J. *Am. Chem. Soc.* **1986**, 108, 7426.
- (20) Engelsberg, M.; Norberg, R. E. *Phys. Rev. B* **1972**, 5, 3395.
- (21) van Vleck, J. H. *Phys. Rev.* **1948**, 74, 1168.
- (22) Lathrop, D.; Franke, D.; Maxwell, R.; Tepe, T.; Flesher, R.; Zhang, Zh.; Eckert, H. *Solid State Nucl. Magn. Reson.* **1992**, 1, 73.
- (23) Eckert, H.; Zhang, Zh.; Kennedy, J. H. *Chem. Mater.* **1990**, 2, 279.
- (24) Eckert, H.; Zhang, Zh.; Kennedy, J. H. *Mater. Res. Soc. Symp. Proc.* **1989**, 135, 259.
- (25) Waugh, J. S.; Fedin, E. I. *Sov. Phys. Solid State* **1963**, 4, 1633.
- (26) Räuber, A. *Curr. Top. Mater. Sci.* **1978**, 1, 481.
- (27) Abrahams, S. C.; Marsh, P. *Acta Crystallogr.* **1986**, B42, 61.
- (28) Kawakami, S.; Tsuzuki, A.; Sekiya, T.; Ishikuro, T.; Masuea, M.; Torii, Y. *Mater. Res. Bull.* **1985**, 20, 1435.
- (29) Birnie, D. P., III. *J. Mater. Res.* **1990**, 5, 1933.